

Research Article

Multiphysics Model of an MR Damper including Magnetic Hysteresis

M. Kubík ¹ and J. Goldasz ^{2,3}

¹Faculty of Mechanical Engineering, Brno University of Technology, Brno, Czech Republic

²Faculty of Electrical and Computer Engineering, Cracow University of Technology, Kraków, Poland

³Technical Center Kraków, BWI Group, Kraków, Poland

Correspondence should be addressed to M. Kubík; michal.kubik@vutbr.cz

Received 12 April 2019; Revised 31 May 2019; Accepted 9 June 2019; Published 26 June 2019

Guest Editor: Efrén Díez-Jiménez

Copyright © 2019 M. Kubík and J. Goldasz. This is an open access article distributed under the Creative Commons Attribution License, which permits unrestricted use, distribution, and reproduction in any medium, provided the original work is properly cited.

Hysteresis is one of key factors influencing the output of magnetorheological (MR) actuators. The actuators reveal two primary sources of hysteresis. The hydro(mechanical) hysteresis can be related to flow dynamics mechanisms and is frequency- or rate-dependent. For comparison, the magnetic hysteresis is an inherent property of ferromagnetic materials forming the magnetic circuit of the actuators. The need for a good quality hysteresis model has been early recognized in studies on MR actuators; however, few studies have provided models which could be used in the design stage. In the paper we reveal a hybrid multiphysics model of a flow-mode MR actuator which could be used for that purpose. The model relies on the information which can be extracted primarily from material datasheets and engineering drawings. We reveal key details of the model and then verify it against measured data. Finally, we employ it in a parameter sensitivity study to examine the influence of magnetic hysteresis and other relevant factors on the output of the actuator.

1. Introduction

Magnetorheological (MR) dampers are fairly well-known devices utilizing MR fluids which, when subjected to magnetic stimuli of sufficient strength, generate yield stress [1]. So far, the unique technology has been commercialized in semiactive passenger vehicle suspensions, powertrain mounts [2], or optical finishing [3]. Low power consumption, fast and reversible responses, and high dynamic range have made the devices attractive for use in vibration control systems in particular [4]. As MR dampers are generally operated in real-time control systems, their dynamic performance is equally important as or more important than their steady-state characteristics. Steady-state characteristics only provide the evidence of an actuator or a damper meeting the required force/torque range (or force/torque) targets. Their dynamic behaviour needs to be quantified at the same time if it is used in a real-life control process. Thus, understanding the contributions of various factors complicating the force or torque build-up dynamic process is critical for the development of a realistic application. Briefly,

with MR actuators, there is ample evidence of several factors complicating the force/torque generation process, namely, mechanical/hydraulic hysteresis, magnetic hysteresis, control circuit dynamics such as eddy currents, driver dynamics, temperature, flow losses, friction, and nonlinear relationship between the material's yield stress and the induced flux [5–7]. These factors influence the device's ability to generate the output force/torque and need to be accounted, for instance, for in the control algorithm development process.

In this study, we pay particular attention to modeling the damper's hysteretic behaviour. In general, MR devices reveal two primary sources of hysteresis. The (hydro-)mechanical hysteresis can be related to the damped dynamics of a heavy slug of MR fluid (MRF) bouncing against compliant columns of MRF in fluid chambers. The effect is rate- or frequency-dependent, and its magnitude varies with the current applied, too. It disappears as the mechanical excitation frequency approaches zero [8]. The magnetic hysteresis is different. It is present in all electromagnetic devices, e.g., electromagnetic solenoids [9], motors [10], and magnetorheological actuators [11]. First of all, it is the inherent

property of ferromagnetic materials forming the magnetic circuit of the MR valve; the hysteresis of carbonyl iron (CIP-) based MFRs is virtually nonexistent [12]. Next, it does not vanish as the inducing current frequency approaches DC limit. Also, temperature, load history, and mechanical stresses have a negative influence on the hysteresis and magnetization characteristics of ferromagnetic materials [13]. For instance, it is a common practice to subject machined ferromagnetic components to heat treatment for internal stress and hysteresis as well as coercive force reduction.

The need for a good quality hysteresis model has been early recognized in studies on MR actuators, and the reader should refer, e.g., to Zheng et al. [14] for a review of suitable phenomenological models as well as to the well-known study of Spencer et al. [15]. In general, the posteriori parametric models were obtained by examining the force-position and force-velocity relationships by fitting by model response to the actuator's output. Such models are suitable for control studies only. In the device's development process, other approaches are required. In that aspect, many MR-related research studies neglected the particular contributor's presence. The topic, however, has been well identified in the field of conventional solenoid actuators where various models were developed to copy the hysteretic behaviour of the actuators. For instance, Mayergoyz [16] applied the Preisach model to model the hysteretic behaviour of a solenoid actuator. In the Preisach model, the hysteresis is the sum of elementary hysteresis loops. Next, Coleman and Hodgdon [17] developed a first-order differential equation that links the field strength H and the flux density B . One model whose parameters can be related to physical properties of ferromagnetic materials is the Jiles–Atherton (J–A) model [18, 19]. The model was extended to include both the impact of eddy currents and temperature on hysteresis and magnetisation curves [20, 21]. All of the above models can be vectorized. Tellinen [22] proposed a simple scalar model for handling the hysteresis based on the limiting hysteresis loop from physical measurements of ferromagnetic materials. With MR actuators, however, although the significance of a good quality hysteretic model has been recognized early, the topic does not seem to have deserved enough attention. Significant contributions include Han et al. [23] who examined the field dependent hysteresis of ER fluids. The authors used the familiar Preisach approach. Moreover, Han et al. [7] used the Preisach model to identify the hysteresis of an MR fluid. Yadmellat and Kermani developed a model of an MR clutch in which the developed hysteresis model was assessed against the Preisach operator [24]. For comparison, in their early study using the Coleman–Hodgdon model, An and Kwon modelled the hysteretic behaviour of an MR clutch, and by examining the torque-current loops showed that the hysteresis is an important contributor to the device's output [25]. The model parameters were identified from physical measurements (of magnetisation characteristics) of the materials forming the magnetic circuit of the clutch. Next, Jędrzycka et al. presented a finite-element (FE) model of an MR clutch based on the J–A approach [26]. Moreover, Guo et al. presented a transient multidomain model of a

flow-mode damper based on the J–A approach and then verified it against the novel FE vector hysteresis technique [27]. The inverse J–A model was recently examined by Zheng et al. [14] to copy the transient behaviour of an MR flow-mode damper. Goldasz et al. [28] proposed an extension of the Bouc–Wen model in an attempt to separate the magnetic hysteresis from the mechanical one. The authors proposed a simple lumped parameter model of the actuator including a hysteretic operator. The model was verified against selected sinusoidal AC excitation inputs and provided acceptable accuracy for practical purposes. Still, when compared to the vast number of research studies using parametric phenomenological hysteretic models, the topic does not seem intensively studied as already mentioned. That may be due to few existing comprehensive electromagnetic models of such actuators.

Another aspect is dynamics. Clearly, the insight into the dynamics of MR actuators should be provided through transient models. Such a comprehensive model would attempt to copy not only the dynamics of the fluid flow through the valve and the flux dynamics but account for the physics outside the control valve as well. Suitable lumped parameter models usually utilize a network of elements representing physical domains of interest (hydraulic, thermal, electric, and magnetic) and connections (interfaces) between them [2]. For example, the electrical circuit of the actuator can be represented in the form of a resistor-non-linear inductor network model [5]. Their main disadvantage is the necessity of using various simplifying assumptions, e.g., uniform yield stress/flux, fully developed flow, etc. On the contrary, continuum multiphysics (magnetics and flow dynamics) models utilize fewer assumptions and can be exercised on realistic geometries, however, at a significant computational expense [29].

As such, in the paper, we propose a hybrid multiphysics model of the magnetorheological damper which separates the magnetic hysteresis of the magnetic circuit of the actuator from that of the mechanical hardware. Briefly, the electromagnetic domain is modelled using the vector hysteresis FE model (present in Ansys Maxwell) based on the extension of well-known Maxwell equations [30], and the hydraulic section is described through dimensionless biplastic Bingham approach [31].

The paper is organized as follows. First, we present an MR damper geometry and key material properties. Then, in the following section, we reveal key details of the FE model of the actuator such as magnetic hysteresis and the coupled lumped parameter hydromechanical model. Next, we show measurements of magnetic hysteresis loops and a comparison of the measurements against the FE electromagnet model. Finally, we show results of a parametric study (also involving the hybrid model) in an attempt to examine the hysteresis influence on the output of the MR actuator and then draw conclusions.

2. Magnetorheological Damper

In the study, an MR flow-mode damper configuration having a single coil assembly in the electromagnet and one annular

flow path in the control valve is of research interest. The damper is presented in Figure 1. The hydraulic tube houses (1) the piston (2), the piston rod (3), the floating piston (4) and the rod guide assembly (5). The piston separates the MR fluid volume into rebound chamber volume and the compression chamber volume. The floating piston separates the fluid from the gas chamber. The MR valve located in the piston control controls the fluid flow between the rebound and compression chamber and vice versa. The MR valve is a conventional control valve by design. It consists of the piston core (6), the sleeve (7), the nonmagnetic flanges or plates (8), the coil assembly (9), and the connecting wires (10) for connecting to an external power supply. It is the most common single-tube MR damper configuration.

The MR valve's magnetic circuit (6, 7) is manufactured out of annealed low-carbon steel 11SMn30 (see the components in blue in Figure 1). The bronze (yellow) flanges (8) define the mutual position of the piston core and sleeve. The distance between the outer diameter of the annulus and the inner diameter of the sleeve defines the annular gap height. The coil assembly (9) incorporates $N = 120$ turns of copper (purple) wire (0.5 mm diameter).

The connecting wires are routed through the thru-hole in the piston rod (3) made of steel 42CrMo4 (AISI 4140). The floating piston, the rod guide, and the remaining components are manufactured out of steel S235JR (green). The MR damper is filled with the fluid MRF132-DG by Lord Corp; see the magnetisation curve in Figure 2(c). The damper key dimensions, rheological properties of MR fluid, and gas chamber details are shown in Table 1. The magnetisation curves of the annealed low-carbon steel 11SMn30 were determined using the measurement system Remagraph C-500. The obtained virgin & hysteresis data can be seen in Figures 2(a) and 2(b).

The coercivity and remanence of the 11SMn30 material sample were determined from the measured hysteresis: $H_c = 209$ A/m and remanence $B_r = 1.09$ T. The material's bulk conductivity was set at 5.8 MS/m. Based on similar measurements of the rod material (42CrMo4), we set its coercivity to $H_c = 1250$ A/m and the bulk conductivity to 4.5 MS/m.

3. Modeling

In the section, we present modeling details. Specifically, we highlight the transient magnetic FE model of the MR valve including hysteresis followed by a description of a monotube damper lumped parameter model. The lumped parameter model is coupled with the transient FE model through the yield stress-flux density interface. We consider the integrated model as illustrated in Figure 3. In the presented layout, the electromagnetic circuit (described in Section 3.1) is driven by the voltage u supplied by the current driver. The resulting output flux density B_g is then converted into the materials' (fluid) field-induced yield stress τ_0 (extracted from the material's datasheet or rheological measurements). Given the input velocity v_r or displacement and the yield stress, we then calculate the output force according to the equations in Section 3.2.

3.1. Transient Magnetic Model with Magnetic Hysteresis. To model the electromagnetic circuit of the MR valve, we applied the vector hysteresis modeling feature available in Ansys Maxwell R19. For isotropic material and 2D/3D problems, the vector play model was recognized to be more computationally efficient than a vector Preisach model [30, 33]. In general, the play model assumes a decomposition of the applied field H into the reversible component H_{re} and the irreversible one H_{ir} . Then, the resulting flux density

$$B = B_{re} + B_{ir} = \mu_0 M(H_{re}) + \mu_0 H_{ir}, \quad (1)$$

where B_{re} is the reversible component of flux density and B_{ir} is the irreversible component. The magnetization M varies with the reversible field component along an anhysteretic curve. The process can be visualized as in Figure 4. The parameters for the model can be identified from the major hysteresis loop. The major hysteresis loop incorporates two branches, the ascending branch and the descending branch, and they can be calculated from each other, the Maxwell model utilizes only one branch of particular B - H loops. The algorithm for constructing the major and symmetric minor hysteresis loops is given in [34].

To develop the FE model, we assumed the valve to be axially symmetrical around the centerline in a cylindrical coordinate system. The geometry of the MR damper piston (valve) was simplified for the transient simulations (Figure 5(a)). The discretized model can be observed in Figure 5(b). As shown, the geometry was discretized using triangular elements. The element length-based refinement with the maximum length of 0.5 mm was applied to the coil core and the sleeve. Next, the value of 0.7 mm was applied to the piston rod and the hydraulic tube, and the criterion of 0.2 mm was applied to the MR fluid region in the active zone.

To accomplish transient field simulations, the FE model was coupled to the external circuit revealed in Figure 6(a). The lumped circuit documents an ideal current source (input) in series with a resistor (coil winding) and the FE valve object (as represented by the nonlinear inductor). The model is subjected to prescribed current waveforms, and the resulting flux density in the annulus B_g is extracted from the simulation results. The flux density B_g presented in the next sections was calculated by averaging flux density of the middle of the annulus. The information is required for coupling the FE model with the damper hydraulics.

The figure also shows the curve fit to the experimental data for the steel 11SMn30 (Figure 6(b)). The agreement is satisfactory except for low magnetic field strength and on the initial magnetization curve only. The core and sleeve components were assigned the B - H properties of the 11SMn30 alloy and the MRF component that of MRF132-DG available from Lord Corp. Also, the rod component was assigned the material properties of the 42CrMo4 steel alloy as mentioned above. Finally, all data in subsequent simulations were obtained using the fixed step-size solver with the following settings: constant time step was 0.05 ms, nonlinear residual was $1e-7$, time integration method was Backward Euler.

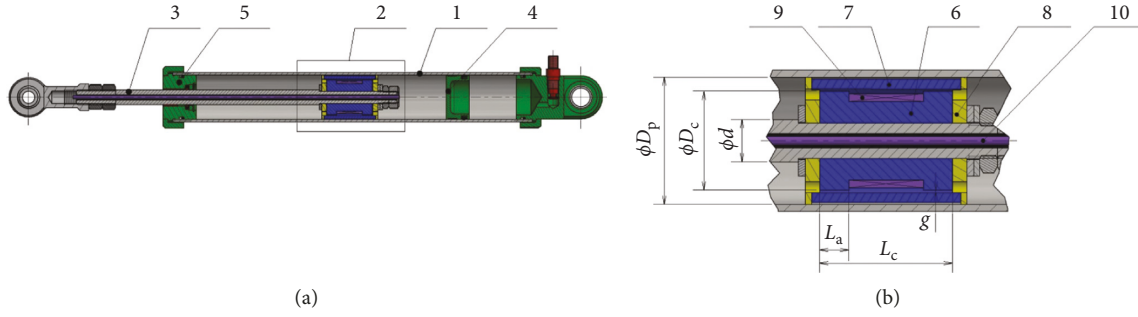


FIGURE 1: Magnetorheological damper. (a) MR damper. (b) Piston (control valve).

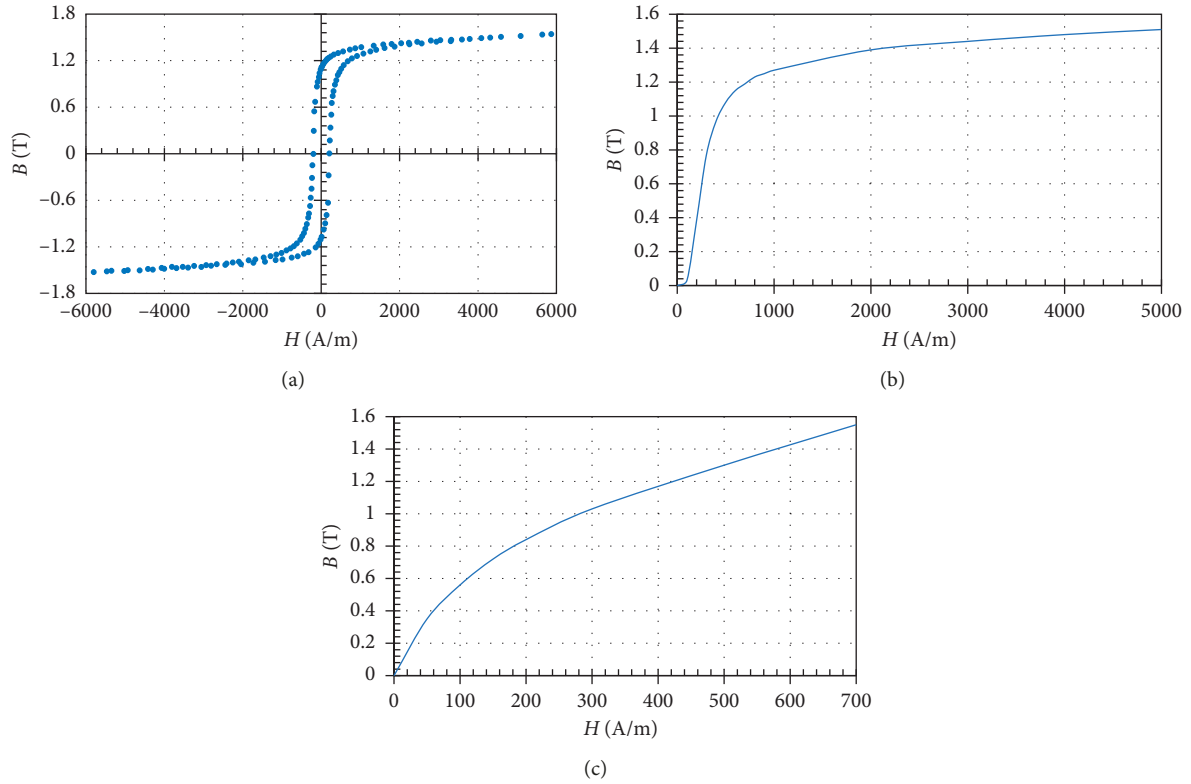


FIGURE 2: Virgin and hysteresis magnetization curves. (a) Hysteresis curve of 11SMn30. (b) Static curve of 11SMn30. (c) Static curve of MRF 132-DG [32].

TABLE 1: MR damper dimensions and material properties.

| Name | Value | Symbol | Unit |
|---|-------|---------|--------------------|
| <i>Geometry and weight</i> | | | |
| Piston rod outer diameter | 12 | d | mm |
| Piston outer diameter | 36 | D_p | mm |
| Annular gap height | 0.65 | h | mm |
| Active zone length | 16 | L_a | mm |
| Core length | 37 | L_c | mm |
| Piston stroke | 150 | L_s | mm |
| Internal diameter of the gap | 28 | D_c | mm |
| Floating piston weight | 0.07 | m_f | kg |
| <i>MR fluid properties (MRF-132DG [32])</i> | | | |
| MR fluid viscosity at 40°C | 0.114 | μ | Pa·s |
| MR fluid isothermal bulk modulus | 1500 | β | MPa |
| MR fluid density | 3090 | ρ | kg·m ⁻³ |

TABLE 1: Continued.

| Name | Value | Symbol | Unit |
|---|-------|----------|--------------------|
| Air content in the MR fluid | 0.01 | α | — |
| <i>Gas chamber</i> | | | |
| Gas volume (at midstroke) | 46000 | V_{g0} | mm^3 |
| Gas temperature | 40 | T | $^{\circ}\text{C}$ |
| Initial gas pressure | 30 | P_{g0} | bar |
| Initial floating piston position | 20 | x_g | mm |
| <i>Others</i> | | | |
| Initial rebound chamber (upper) MR fluid volume | 63333 | V_{r0} | mm^3 |
| Initial compression (lower) chamber MR fluid volume | 71250 | V_{c0} | mm^3 |
| Coil turns | 120 | N | — |
| Coil resistance | 1.0 | R_c | Ω |
| Nondimensional viscosity ratio (est.) | 0.1 | γ | — |
| Yield stress number (est.) | 0.5 | δ | — |

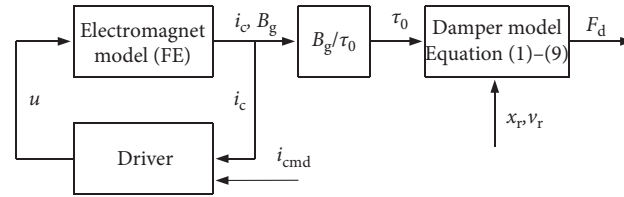


FIGURE 3: Block diagram of the proposed model.

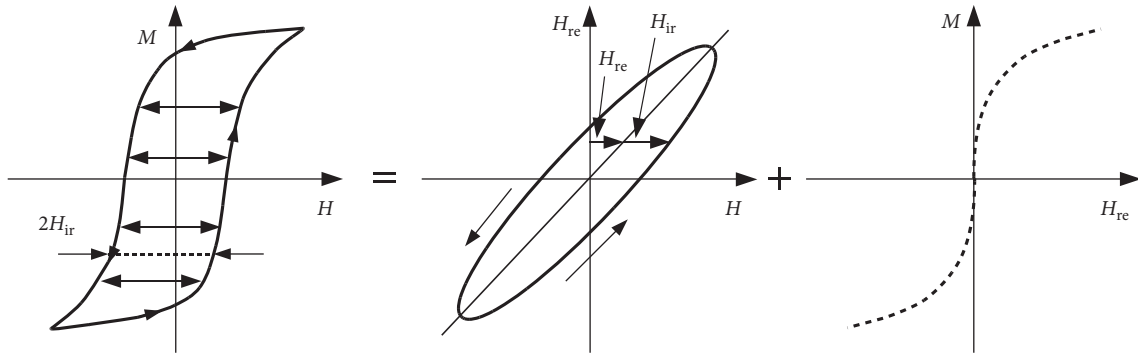


FIGURE 4: Magnetic field decomposed into reversible/irreversible components [35].

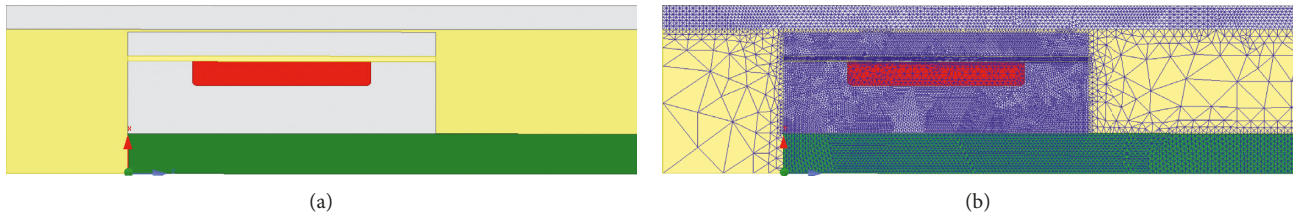


FIGURE 5: Simplified geometry of the piston unit and mesh. (a) Geometry. (b) Mesh.

3.2. Hydromechanical Model. To illustrate or reveal the effect of fluctuating (transient) magnetic field on the output of the actuator, a capable damper model is required. Modeling the behaviour of MR dampers has been clearly the subject of intensive research, to name only [36–38]. However, we chose to proceed further with the model of Goldasz and Sapinski in [2]. The approach is flexible, incorporates most key physical

phenomena occurring in the MR valve and outside of it, and was successfully verified against several MR piston valve configurations (monotube damper, valve: single coil, single annular flow path, magnetic flux bypass feature). Therefore, in the sections that follow, we describe details of the lumped parameter model of the damper and the coupling method with the FE transient model.

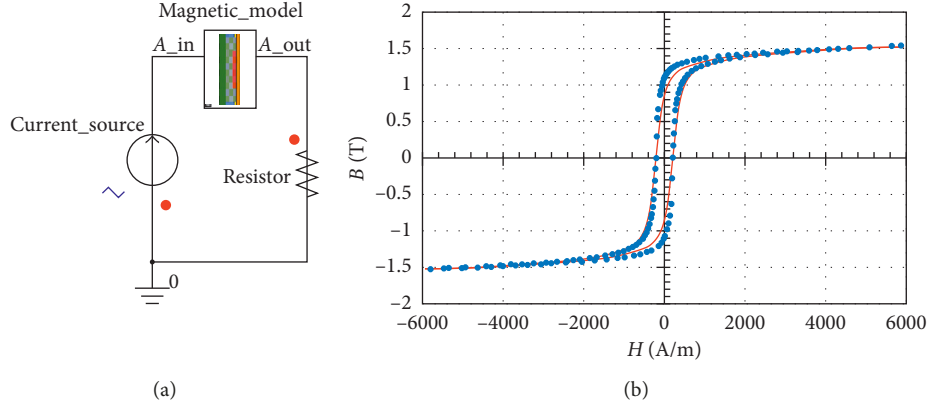


FIGURE 6: External circuit model and magnetisation curve: 11SMn30 (curve fit vs data). (a) External circuit. (b) B - H plot.

3.2.1. MR Damper Model: Theoretical Background. The schematic geometry of the damper is revealed in Figure 7. In the presented illustration, the piston separates the upper (rebound) fluid chamber from the fluid below it (compression chamber). The pressure in the upper chamber is P_r , and its (initial) volume is V_r (V_{r0}). Accordingly, the pressure in the compression chamber is P_c , and its (initial) volume is V_c (V_{c0}). The gas pressure is P_g (P_{g0}), and the (initial) gas volume below the floating piston is referred to as V_g (V_{g0}). At static conditions, the pressure in each chamber is equal to P_{g0} . The cross-sectional area of the piston is A_p and that of the rod A_r . As the piston rod moves, it displaces the floating piston (separating the lower fluid chamber and the pressurised gas). The floating gas cup mass is m_g , and its displacement is x_g . The friction forces against the rod guide and the floating piston are F_{fg} and F_{fr} , respectively. We assume one annular flow path in the MR valve; dimensions: h is the gap height; w is the circumferential width (at perimeter); $A_g = wh$ is the flow channel area. The flow rate through the annulus is referred to as Q_a . Finally, we refer to the displacement of the piston rod as x_r and to that of the cylinder tube as x_t (not shown).

The fluid's behaviour is quantified with the viscosity μ , the density ρ , the compressibility β , and the field-induced yield stress τ_0 . The non-Newtonian rheology of the MR fluid is described using the biplastic Bingham model [31].

We assume that the damper model would account for the following phenomena: MR effect (using the biplastic Bingham model mentioned above), compressibility of fluid, dynamics of the fluid element ("slug") motion when forced through the annulus, entrance and exit losses in the annulus, floating piston mass inertia, and seal friction. Elasticity of the cylinder tube, various effects due to heating, and the dependency of seal friction on the damper internal pressure are not accounted for.

First, the gas pressure in the volume below the floating piston can be modeled by assuming the adiabatic process ($n=1.4$). The gas pressure P_g is then dependent on the position of the floating piston x_g in the following manner:

$$P_g = P_{g0} \left(\frac{V_{g0}}{V_{g0} + A_p x_g} \right)^n. \quad (2)$$

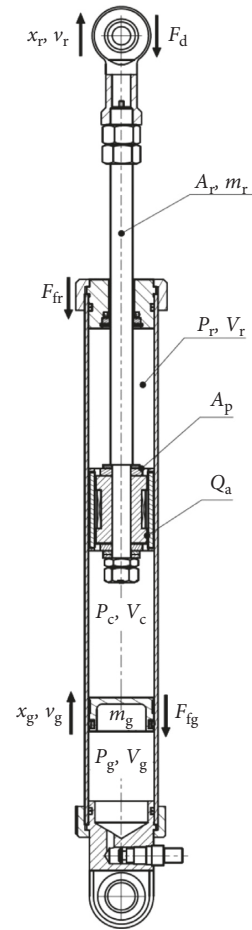


FIGURE 7: Damper model schematic layout.

The pressure variation in the chambers below/above the piston is modeled assuming isothermal processes and the conservation of mass approach [39]. Next, the dynamics of the mass of fluid is considered by examining the motion of the fluid mass in the annular channel. The resulting system of ordinary differential equation in the state-space form which describes the mutual relationships between the rebound pressure chamber P_r , the compression chamber pressure P_c , the floating piston motion velocity v_g , and the

volumetric flow rate through the annulus Q_a is shown below

$$\dot{P}_r = \beta \frac{(A_p - A_r)v_p - Q_a}{V_r}, \quad (3)$$

$$\dot{P}_c = \beta \frac{(v_g - v_p)A_p + Q_a}{V_c}, \quad (4)$$

$$\dot{v}_g = \frac{1}{m_g} [A_p(P_c - P_g) - F_{fg} \text{sign}(v_g)], \quad (5)$$

$$\dot{Q}_a = \frac{A_g}{\rho L} (P_r - P_c - \Delta p_a). \quad (6)$$

As already mentioned, the behaviour of the energized MR fluid is described by incorporating the field-dependent losses into the pressure drop Δp_a which is described in detail in Section 3.2.3; the reader should refer to [2, 39] for a more detailed derivation of the equations and the experimental verification method. The pressure term also incorporates the local flow losses Δp_e . The local flow losses as the fluid enter/exits the annulus are accounted for using the semiempirical equation [40]:

$$\Delta p_e = K \frac{\rho Q_a}{2A^2} |Q_a|, \quad (7)$$

$$K_{SE} = K_{cor} \left(1 - \frac{A_g}{A_p}\right)^2, \quad (8)$$

$$K_{SC} = K_{cor} \left(1 - \frac{A_g}{A_p}\right)^{0.75}, \quad (9)$$

where K/K_{SE} is the pressure loss coefficient for the sudden enlargement (exit from the gap), K/K_{SC} is the pressure loss coefficient for the sudden contraction (entrance to the annular gap), and K_{cor} is the correction factor. Finally, considering the forces acting on the piston yields the following relationship:

$$F_d = (A_p - A_r)P_r - P_c A_p + F_{fr} + F_{fg}. \quad (10)$$

The friction force in MR damper is assumed to be the sum of Stribeck, Coulomb, and viscous components [40]. As already mentioned, the effects of viscosity change with temperature (heating) are not included.

We solve the system of equations (2)–(10) using the multidomain modeling package Simscape which extends Simulink with tools for object oriented modeling and simulating multiphysics systems [40]. Our model as shown in Figure 8 consists of mechanical, hydraulic, and physical signals domains. Using that environment, the MR damper model was developed with isothermal hydraulic double-acting cylinder components, adiabatic gas blocks, and friction components. The MR fluid behaviour as copied specifically by equation (6) was defined by means of a custom component based on the biplastic

Bingham model approach [31] in series with the local loss model.

To allow simulations of the transient performance of the damper, the model was coupled to the FE model in Ansys Maxwell through the magnetic flux density vs yield stress relationship, $\tau_0 = \tau_0(B_g)$. The interface assumes zero delay between the electromagnetic response of the circuit and the MRF response. MRF measurements indicate the response time of the fluid to be below 0.6 ms; therefore, that particular contribution is omitted in the developed equation set.

3.2.2. Magnetorheological Valve Model. In this section, we describe the biplastic Bingham computing scheme for determining the pressure drop across the magnetorheological valve. Specifically, the relationship between the flow rate through the annulus Q_a and the pressure drop Δp_a is needed. The biplastic scheme is preferred rather than the conventional Bingham approach as it is more flexible and allows for a more effective modeling of low velocity features in the annulus, e.g., magnetic bypass [2]. Using the dimensionless representation of the scheme in terms of the pressure number G and the plasticity S , we express the relationship between the flow rate Q_a and the pressure drop across the annulus Δp_a as

$$\Delta p_a = \frac{2\tau_2 L_a}{h} G(S) = \frac{2\tau_0 L_a}{h(1-\gamma(1-\delta))} G(S), \quad (11)$$

where

$$\begin{cases} G = -\frac{h\Delta p_a}{2L_a\tau_2}, \\ S = \frac{12\mu Q_a}{wh^2\tau_2}. \end{cases} \quad (12)$$

The two additional parameters, γ and δ , are referred to as the artificial viscosity ratio and the (nondimensional) bypass number (yield stress ratio), respectively. As the biplastic model was well studied in prior research papers, the reader should refer there for in-depth details and the parameter estimation method. Briefly, δ controls the intercept force at the zero piston velocity, and γ influences the curve's slope below the knee-point of the force-velocity characteristics [2]. The two parameters of the biplastic model are related to the valve's geometry rather than material properties. The estimation procedure was highlighted, e.g., in [36]. For example, based on prior knowledge, the value of δ (0.5) was selected for a valve with no leakage flow path in the annulus. Using the model, we classify the valve's behaviour into two flow regimes: preyield ($G \leq 1$) and postyield ($G > 1$). The transition point coordinates at which the behaviour of the pseudomaterial changes from the preyield regime to the postyield regime are equal to $G = 1$, $S_0 = \gamma(2 - 3\delta + \delta^3)$. Briefly, when in the postyield regime, the relationship between G and S can be expressed as

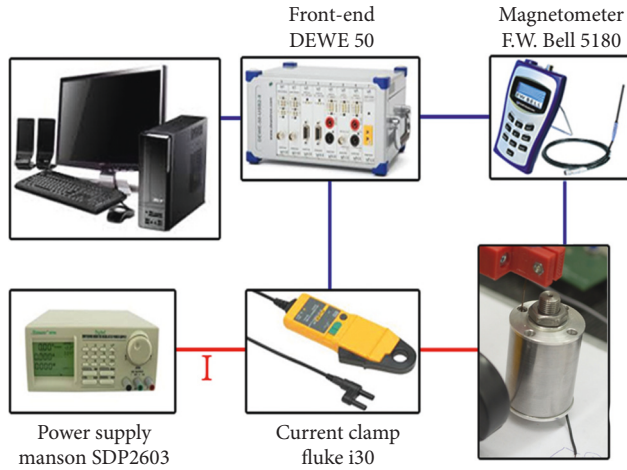


FIGURE 9: Test rig configuration.

Step 2, and (5) repeat Step 1. Using the highlighted procedure, the magnetic flux density was measured for the maximum current levels $I_{\max} = \{0.5, 1, 2, 3, 4, 5\}$ A, respectively.

The measurements of magnetic flux in the annular gap were performed without the MR fluid. Note that the relative permeability of the Hall sensor ($\mu_r = 1$) placed in the thin annulus with MR fluid would distort the accuracy of the experiment as the flux flows around the probe as illustrated in Figure 10. In the simulations, we assume the presence of MR fluid would not degrade the accuracy of the model.

4.2. Results. The obtained data are revealed in Figure 11 as plots of flux density vs coil current.

Observations of the plots of flux density vs current reveal the presence of hysteresis and nonlinear behaviour with the actuator approaching the saturation at the highest current level ($I_{\max} = 5$ A).

5. Modelling Results

The series of modelling experiments was split into two stages. First, we validate the transient FE model against the experimental data, and then we study the behaviour of the hydraulic model.

5.1. FE Model Verification: Air Gap, No MR Fluid. Here, the FE model of the damper described in Section 3.1 was verified against the obtained air gap flux density measurements. The comparison of the obtained data against the model output can be observed in Figure 12 as plots of flux density vs coil current. Due to the low current change rate, the eddy currents were neglected in the model, and only the hysteresis contribution was studied.

Again, observations of the plots reveal satisfactory agreement with the model anywhere except for the smallest exciting current. Overall, the plots prove the rationality of the proposed approach.

5.2. Hysteresis Assessment of the MR Valve. Due to reasons explained in Section 4.1, direct assessment of the hysteretic behaviour of the MR valve with the fluid in the annulus was not possible with the available laboratory equipment. However, CIP- (carbonyl powder iron-) based MR fluids show virtually zero hysteresis [12]. Therefore, the presence of the fluid in the annulus only modifies the flux density-current relationship through its (nonlinear) magnetisation characteristics. Hence, it is reasonable to proceed further under the assumption that electromagnet model of the actuator was validated, and it would be accurate also in the scenarios in which the MR annulus would be filled with the fluid. Due to the magnetic circuit saturation above 2 A, we reveal the results for the exciting currents up to 2 A (Figure 13). The nonlinear contribution of the fluid is evident in the presented results.

Next, we examine the behaviour of the valve model for the two following variants:

- (i) Hysteresis (core loss) ON, eddy currents ON (solid line)
- (ii) Hysteresis (core loss) ON, eddy currents OFF (dashed line)

The hysteresis model was applied to all 11SMn30 components (core, sleeve). As presented in Figure 14, the calculated remanent flux density is relatively independent of the previous magnetic history within the examined coil current range from 0.5 A to 2 A, and the effect of eddy currents is rather insignificant in the examined case as already revealed in Figure 14.

Furthermore, we repeated the flux density calculations for one selected electric current level ($I_{\max} = 2$ A) for the following three model variants:

- (i) Hysteresis switched OFF, eddy currents switched OFF (dashed line)
- (ii) Hysteresis ON, eddy currents OFF (dotted line)
- (iii) Hysteresis ON and eddy currents ON (solid line)

The results are revealed in Figure 15. It is now apparent that the hysteresis has the biggest impact on the initial

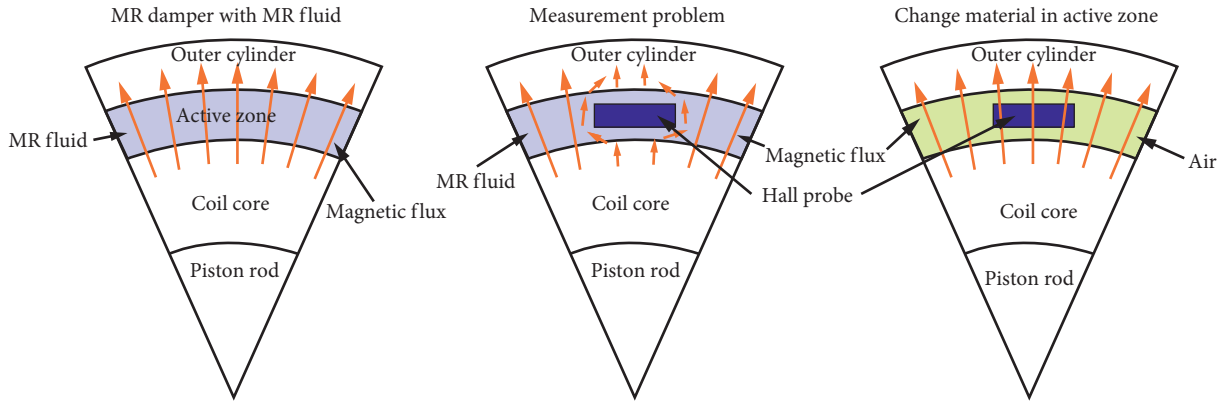


FIGURE 10: Illustration of the measurement problem with Hall sensor in the annular gap in the presence of MR fluid [41].

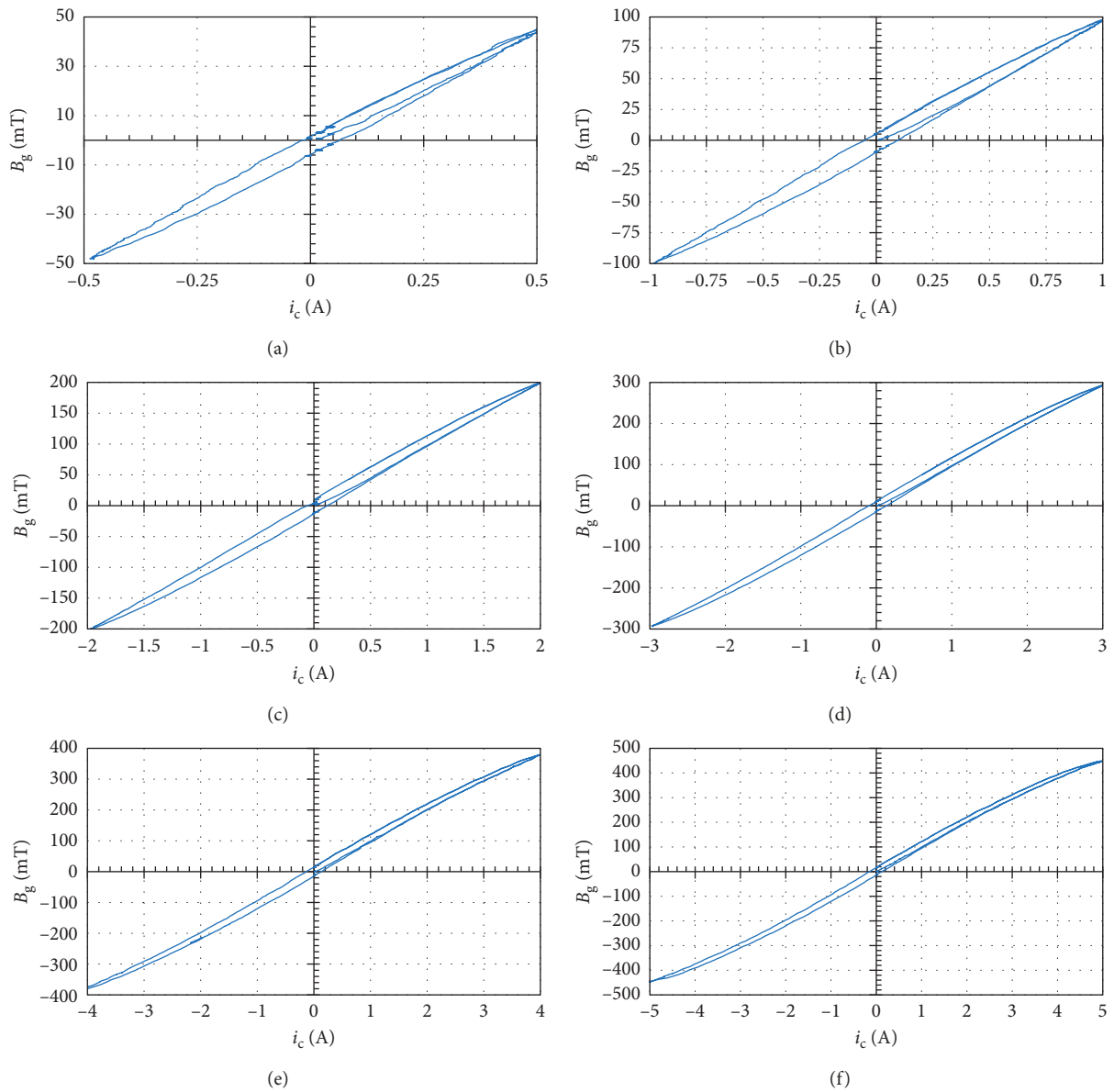


FIGURE 11: Flux density measurements: air gap, no MR fluid. (a) $I_{\max} = 0.5$ A. (b) $I_{\max} = 1.0$ A. (c) $I_{\max} = 2.0$ A. (d) $I_{\max} = 3.0$ A. (e) $I_{\max} = 4.0$ A. (f) $I_{\max} = 5.0$ A.

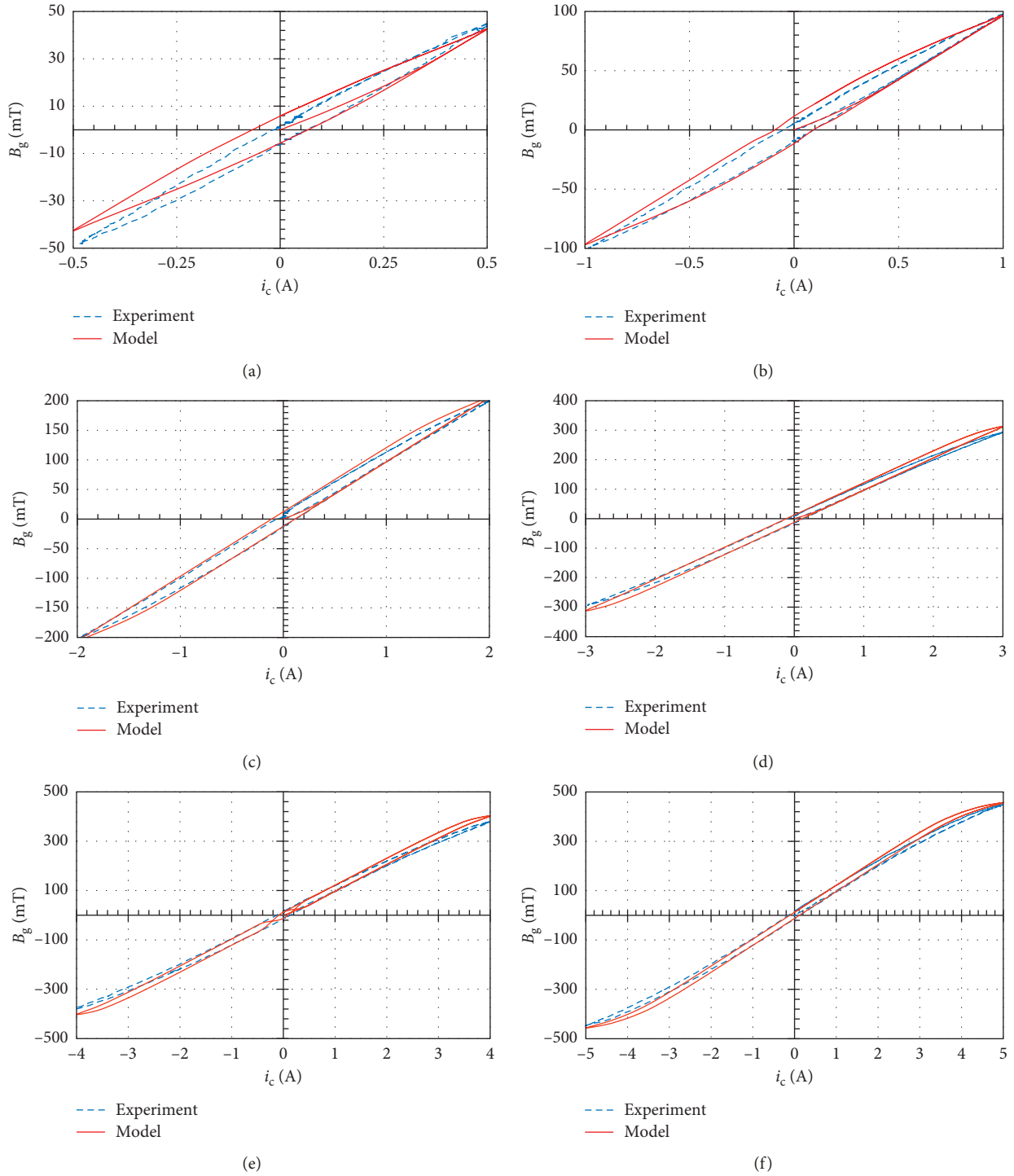


FIGURE 12: Air gap flux density: measurements vs FE model. (a) $I_{max} = 0.5$ A. (b) $I_{max} = 1.0$ A. (c) $I_{max} = 2.0$ A. (d) $I_{max} = 3.0$ A. (e) $I_{max} = 4.0$ A. (f) $I_{max} = 5.0$ A.

output of the actuator (up to 100 mT), and the contribution of the eddy currents is negligible within the examined time scale. The eddy currents have little effect on the output flux density in the examined case (Figure 15). Clearly, the first and second scenarios are only hypothetical ones and unseen

in real MR devices. However, they were included in the simulation for the purpose of isolating the contribution of a specific phenomenon.

Now, the obtained flux density output can be converted into the resulting yield stress and then used in all subsequent

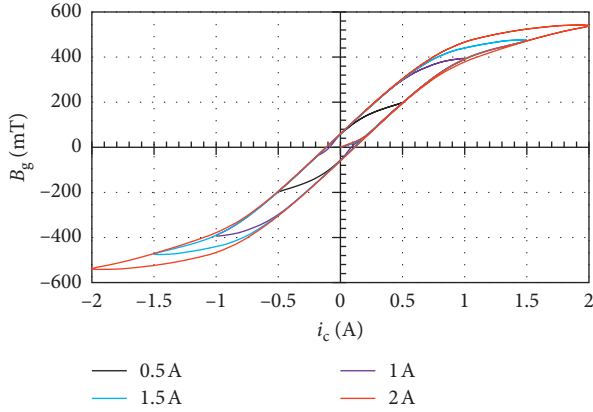


FIGURE 13: MR fluid contribution: calculated flux density vs. exciting current.

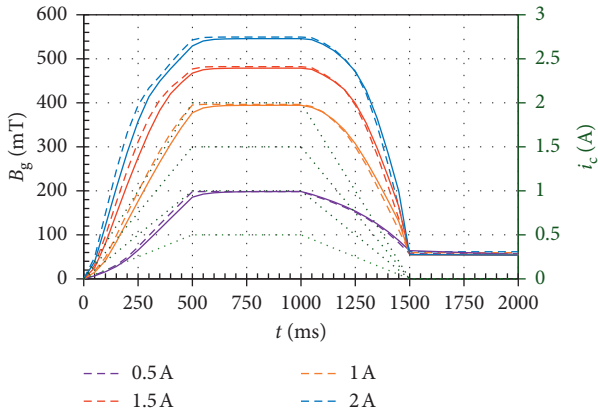


FIGURE 14: Time history of (gap) magnetic flux density: hysteresis ON (dashed line), hysteresis ON and eddy currents OFF (solid line), and electric current (dotted line).

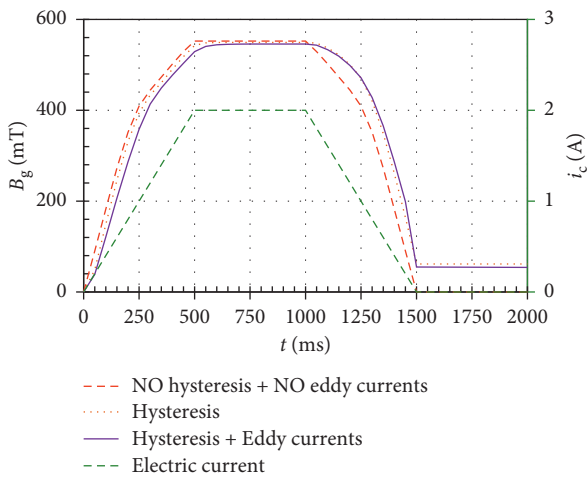


FIGURE 15: Time history: (gap) magnetic flux density, $I_{\max} = 2$ A.

damper simulations (Figure 16). As seen in the calculated data, the residual flux results in the field-induced yield stress of appr. 2.23 kPa.

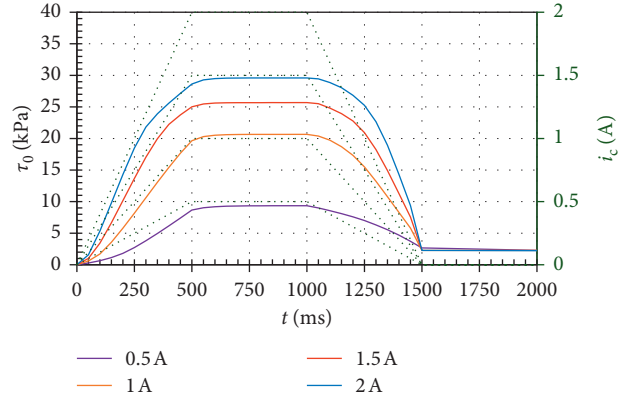


FIGURE 16: Time history: yield stress (full line) and electric current (dotted green line).

5.3. Damper Response to Sinusoidal Displacement Inputs.

Using the set of equations (1)–(9) in Section 3.2.1 and (10)–(16) in Section 3.2.2 as well as the above yield stress map in Figure 16, we then modelled the response of the damper subjected to sinusoidal displacement inputs at fixed (constant) current levels. This was merely for demonstrating the force output of the damper corresponding to the prescribed current levels. The calculated results are highlighted as plots of force vs velocity and force vs displacement for the peak velocity $V_r = 0.3$ m/s in Figure 17. In the calculated example, the stroking amplitude X_r was 30 mm. Note that the data are shifted by the gas force proportional to the product of the gas pressure P_g and the piston rod area A_r (equal to 339 N). Hysteresis due to compressibility of the fluid (increasing with the current/flux level), force oscillations at piston motion reversal points, can be also observed in the generated plots, too.

Moreover, the influence of remnant flux can be seen in Figure 18. In the figure, we present the results of off-state (zero current) simulations with and without demagnetization cycle. In the revealed example, the damper was subjected to a sinusoidal displacement input at the peak velocity $V = 0.3$ m/s. The blue loops reveal the damper response after demagnetization, and the red loops copy the off-state behaviour of the damper which was previously excited at $I_{\max} = 2$ A. The presence of the remanent flux (appr. 54 mT) results in the contribution of 140 N.

5.4. Damper Response to Control Current Step Inputs.

The optimal performance of a S/A (semiactive) control system with an MR damper requires understanding its dynamic behaviour. In controller design studies as well as vehicle simulation, a need for modeling the MR damper system dynamics arises quite often; the time delay between the force and the control signal due to, e.g., eddy currents degrades the system performance. Therefore, in this section, we reveal the results of a series of simulations in which the influence of eddy currents, magnetic hysteresis, and hydromechanical hysteresis (due to compressibility of the fluid) is considered. In the simulations, we assumed a fast controller [6] capable of driving the coil to within 2 ms of the commanded values.

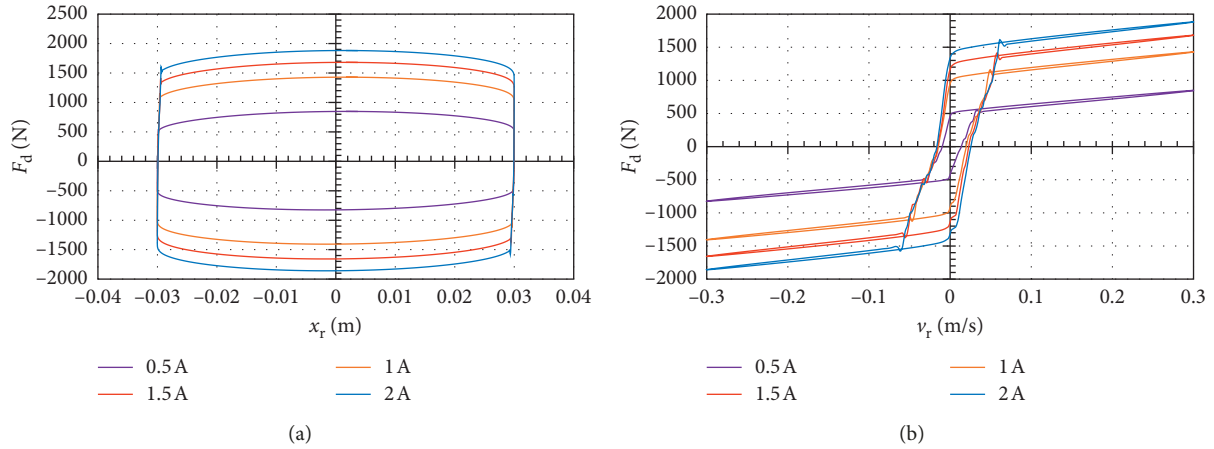


FIGURE 17: Fixed current: force vs. velocity and force vs. stroke, $V_r = 0.3$ m/s. (a) F_d vs x_r . (b) F_d vs v_r .

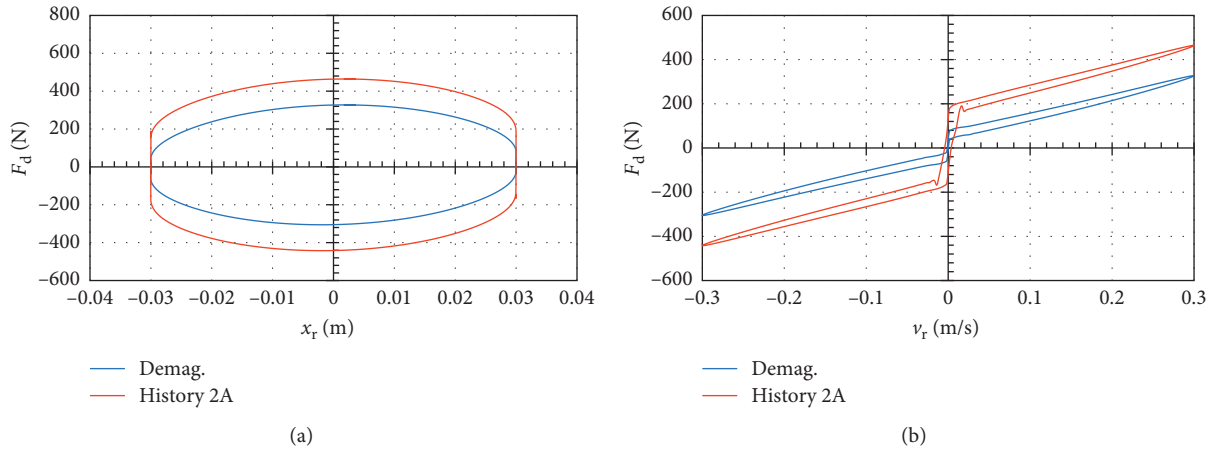


FIGURE 18: Off-state force: demagnetized (blue) and following 2 A current excitation, no demagnetization (red). (a) F_d vs x_r . (b) F_d vs v_r .

The output is highlighted in Figure 19. As seen, the actuator’s off-state output is degraded by the presence of a static (residual) flux. The actuator is capable of reaching zero flux only in the hysteresis-free scenario.

In Figure 20, we further examined the force output varying the coercivity from 0 A/m to 200 A/m. It has no effect on the force output in the current (flux) rise stage; however, in the current drop case (Figure 20(b)), its contribution became evident as the actuator never reached the initial force of 240 N (prior to the current excitation).

5.5. Sensitivity to Gap Height: Parametric Study. Next, the following series of numerical experiments involved studying the contribution of the MR valve’s geometry on the residual force (and flux) output. The model setup incorporated the hysteresis loss model only and no eddy current mechanism. Throughout the experiment series, the coercivity H_c was varied from 120 A/m to 600 A/m, and the gap size h from 0.65 mm to 1.0 mm. The generated B - H loop set (core material) is revealed in Figure 21.

The calculated results are shown in Figure 22 for the maximum electric current of 2 A. The exciting current input

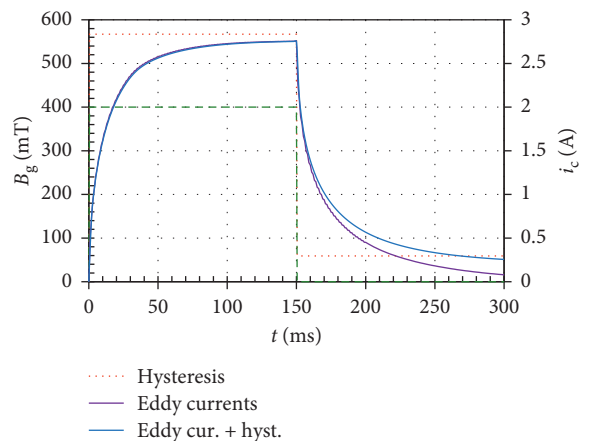


FIGURE 19: Transient FE model: time history of magnetic flux density and electric current (dashed green line).

is identical with that in Figure 14. The coercivity influences the course of the magnetic flux density over time. The greater the coercive force applied, the slower the slope of magnetic induction observed. Moreover, the material coercivity also affects the maximum achievable magnetic flux induction.

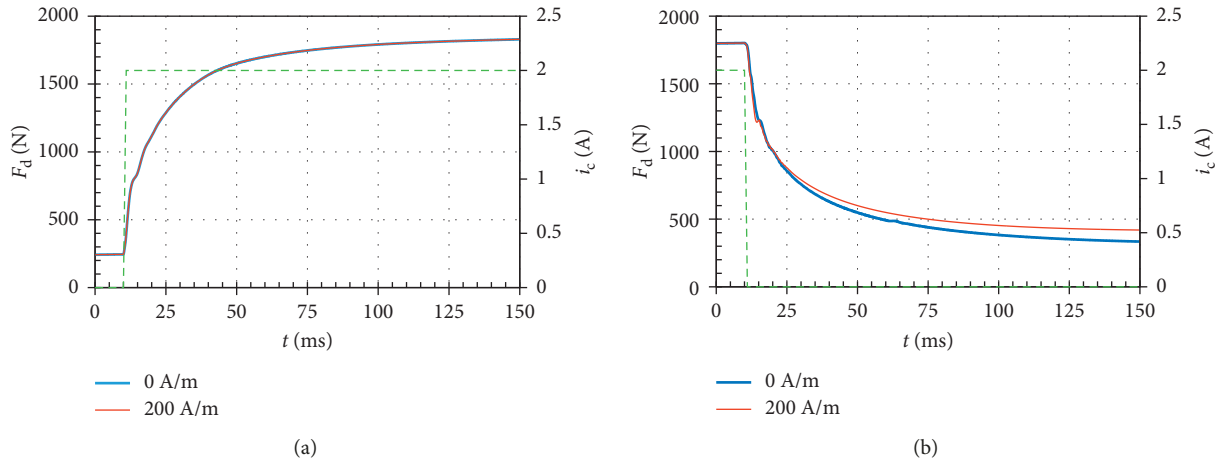


FIGURE 20: Force time history: damper response to current step input, $I_{\max} = 2$ A (electric current course highlighted by the green dashed line). (a) Current rise. (b) Current drop.

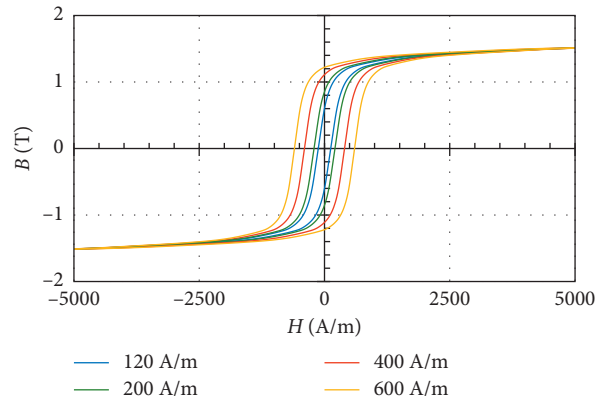


FIGURE 21: Coercivity: impact on the core material magnetisation characteristics (11SMn30).

Note that the greater the coercive force, the lower the maximum magnetic flux density generated. However, the difference is minor on the order of several percent. The difference in maximum magnetic flux density can also be due to the different shape of the generated hysteresis B - H curve by Ansys Electronics. This effect will have to be further studied in follow-up research. However, one other conclusion can be drawn: the remanent flux density follows the coercivity change. The greater the coercivity, the greater the remanent flux density induced.

The relationship of the remanent flux density vs coercivity within the range from 120 to 600 A/m is linear (Figure 23). The remanent flux density decreases as the annular gap height is increased.

Furthermore, it was of research interest to compare the impact of the material coercivity on the ratio B_{\max}/B_{rem} , where B_{\max} is the gap maximum flux density, as there is a significant influence of the annular gap size on the calculated flux density ratio at low material coercivity levels (Figure 24). It is evident that the gap height does not affect the flux density ratio at higher coercivity levels. This ratio follows the turn-up ratio change of the MR damper (Figure 25). The increase of gap size and the coercivity degradation

significantly increase the turn-up ratio K_f of MR damper. However, the maximum damping forces decrease at the same time as illustrated in Figure 26.

5.6. Parameter Sensitivity Study: Transient Response. In this section, we present the results of a parameter sensitivity study. Here, we examine the influence of the coercive force H_c , the electric conductivity σ , and the piston velocity v_r on the damping force under constant velocity excitation ($V_r = 0.3$ m/s) and current step inputs.

5.6.1. Influence of Material Coercivity. To examine the contribution of the coercivity H_c , we simulated the damper model response to current step inputs within the range from 120 A/m to 600 A/m. In each scenario, we assumed the material's electric conductivity σ equal to 1 MS/m (which is typical to some silicon steel alloys or soft magnetic composites) and the presence of eddy currents. The FE results from the transient model are shown in Figure 27. The coil current step input is also shown in Figure 27 (green dashed line).

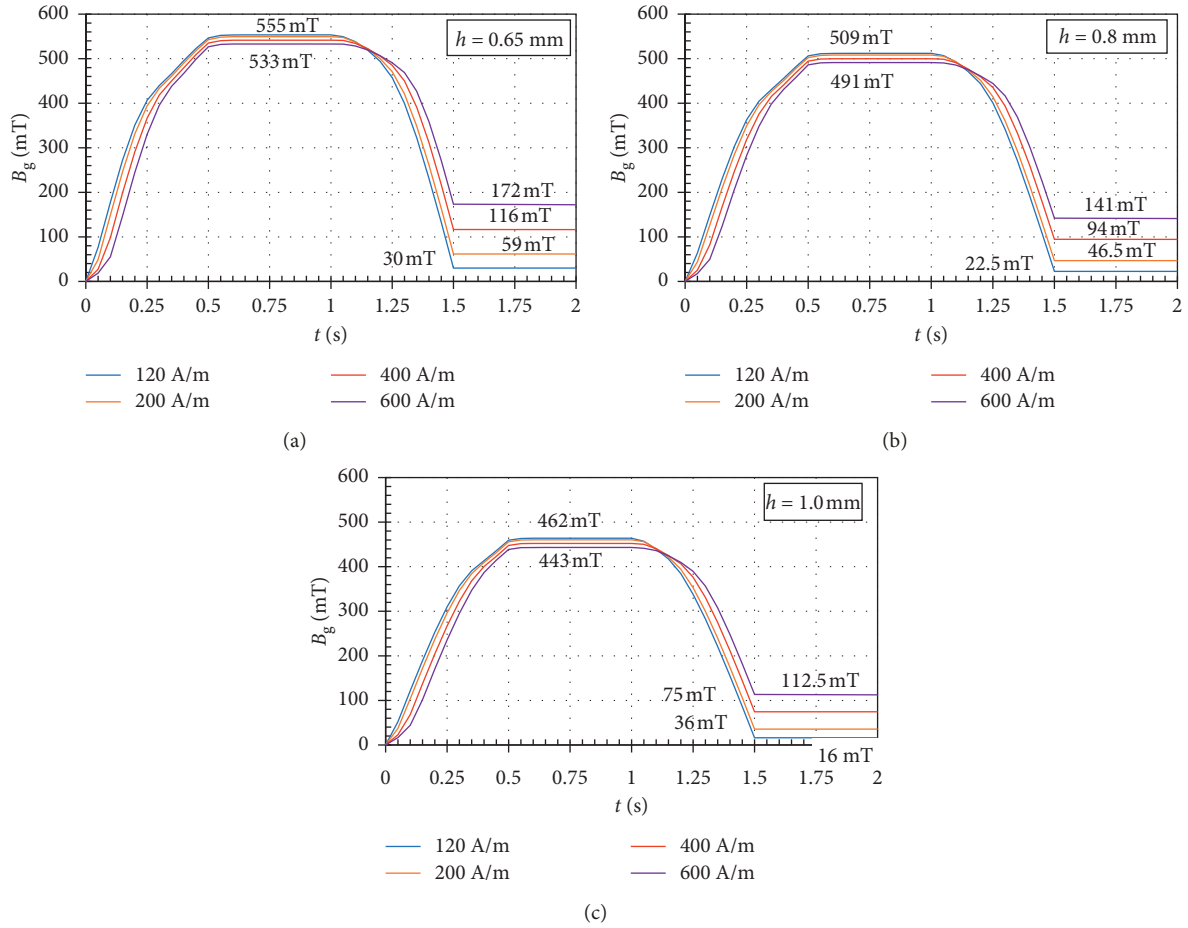


FIGURE 22: Influence of gap height and coercivity on magnetic flux density. (a) $h = 0.65$ mm. (b) $h = 0.8$ mm. (c) $h = 1.0$ mm.

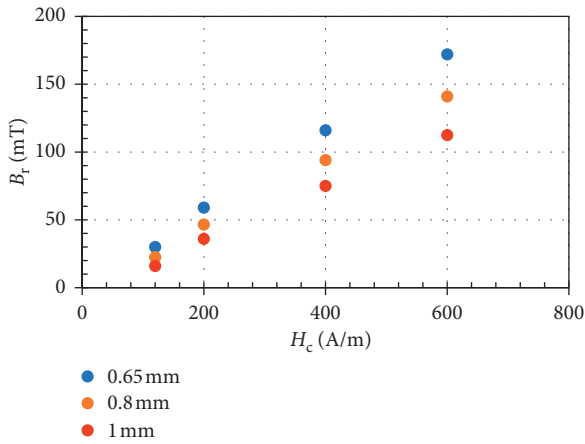


FIGURE 23: Remanent flux density variation with coercivity and gap size.

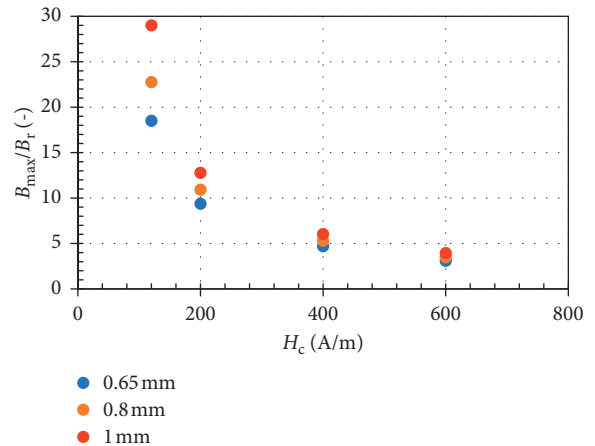


FIGURE 24: Maximum-to-remanent flux density ratio vs material coercivity.

The corresponding time histories of the damping force following the current (flux) rise/decay are revealed in Figure 28.

5.6.2. Influence of Electric Conductivity. It is well known that the ferromagnetic material’s electric conductivity has a rather dramatic effect on the eddy currents induced in

solenoid structures. Here, we simulate the transient response of the damper subjected to 2 A current step inputs. The value of 5.8 MS/m is typical of low-carbon steel alloys, whereas 1 MS/m characterizes some soft magnetic composite materials. The resulting time history is revealed in Figure 29. As shown, as the conductivity decreases, the eddy currents are reduced, and the response of the damper becomes faster.

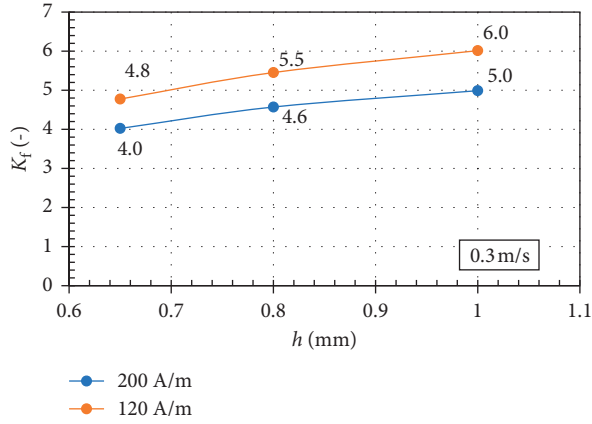


FIGURE 25: Turn-up ratio variation with gap height and coercivity, $V_r = 0.3$ m/s.

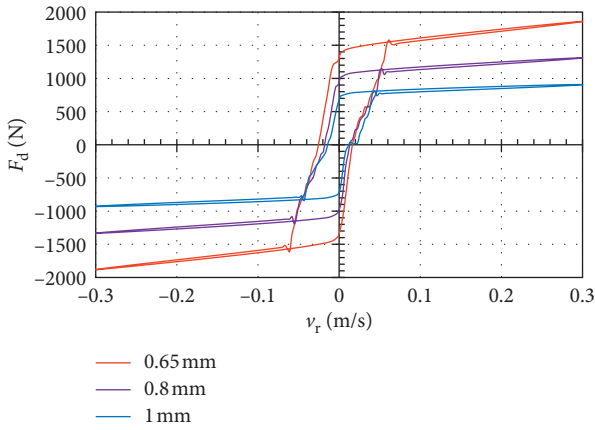


FIGURE 26: Gap height influence on damping force output, $I_{max} = 2$ A $V_r = 0.3$ m/s.

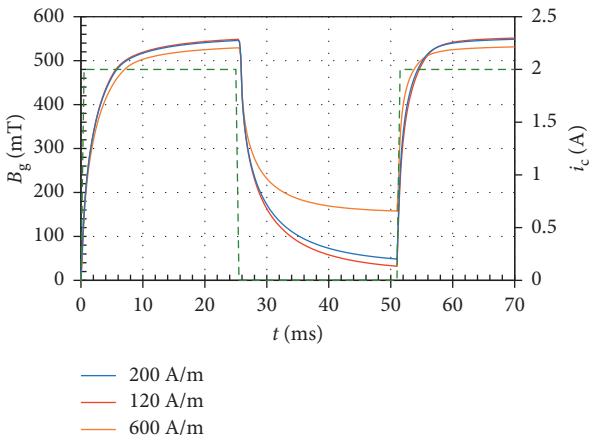


FIGURE 27: Coercivity H_c : (gap) averaged magnetic flux density time history.

5.6.3. Influence of Piston Velocity. Setting the electrical conductivity to 1 MS/m and the coercivity to 200 A/m, we then tested the influence of the piston velocity on the force. In the presented examples, the force output time histories were normalized for better comparison. The obtained results

imply that the slower the piston velocity for control current rise, the slower the magnitude of the force change rate generated. After exceeding the piston velocity of 0.2 m/s, the actuator response in the current rise stage is independent of the piston velocity (Figure 30). However, the exact velocity value will depend on the particular damper design. For comparison, the actuator response in the current drop stage is independent of the prescribed piston velocity.

Apart from the eddy currents, the main source of slower force rise is the compressibility of the MR fluid itself. Three different values of MR fluid bulk modulus were tested to illustrate this effect (Figure 31).

The primary response time of force (63.3% of final force) was calculated from the simulated data (Figure 30) (Figure 32). The primary response time for control current rise is influenced by the piston velocity. The lower the piston velocity, the lower the primary response time. However, the primary response time for control current drop is independent of piston velocity. It is noteworthy that similar trends were experimentally determined in other research studies [42, 43].

6. Conclusions and Summary

In this paper, we present the results of a modeling study involving a multiphysics model of a flow-mode MR damper. The model allows integrating an FE electromagnet model of the device with a hydraulic lumped parameter model of the device. The modeling approach relies only on the information which can be extracted from engineering drawings (geometry), material data sheets (material properties), and therefore, it can be used in studies on the performance of real actuators or virtual prototypes.

The electromagnet was verified experimentally. Based on the obtained data, we conclude that the model is capable of predicting the magnetic hysteretic behaviour of the MR valve. The results concerning the hydraulic model are simulated; however, it should be noted that the model is based on a well-established and experimentally verified theory [39]. To demonstrate the usefulness of the model, we applied it in a parametric study, in which the contribution of various geometric parameters and material properties to the output of the actuator was studied and analyzed. For instance, we can conclude the following.

- (i) Residual magnetic flux is directly related to the current history and the annular gap height
- (ii) Larger annular gaps induce lower remanent (residual) flux density and then less undesired force increase (Figures 22 and 23)
- (iii) Valves with larger annular gaps height reveal higher turn-up ratio (dynamic range), however, at the expense of maximum damping forces (Figures 25 and 26)
- (iv) Turn-up ratio (dynamic range) varies with the coercivity and gap height (Figure 25)
- (v) Demagnetizing current cycles are required to reduce/eliminate the residual flux (and the force increment due to the residual flux)

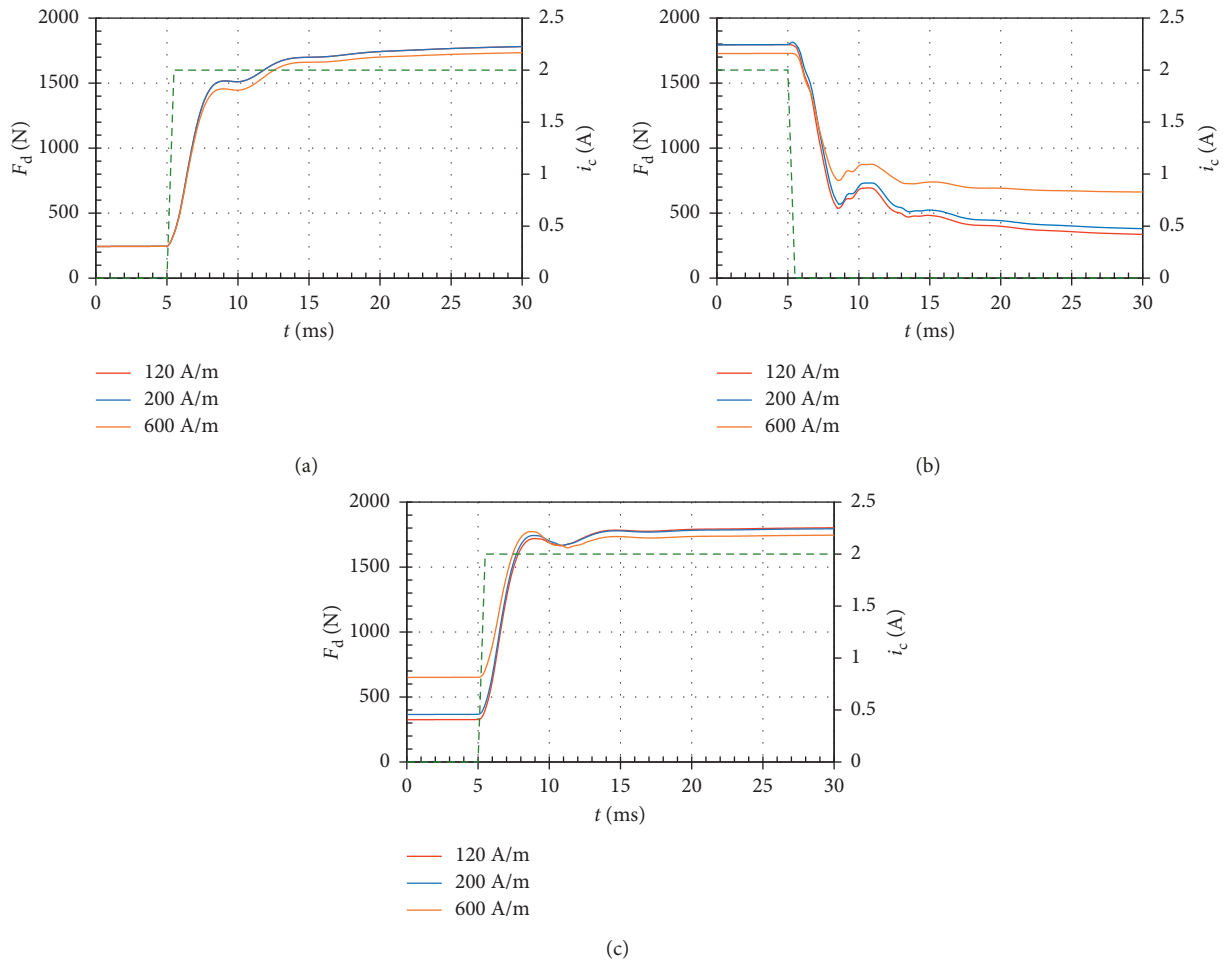


FIGURE 28: Impact of the coercivity H_c . Full line: damping force time history; green dashed line: current step input. (a) Force vs time: current rise (initial condition = demag.). (b) Force vs time: current drop. (c) Force vs time: current rise (no demag.).

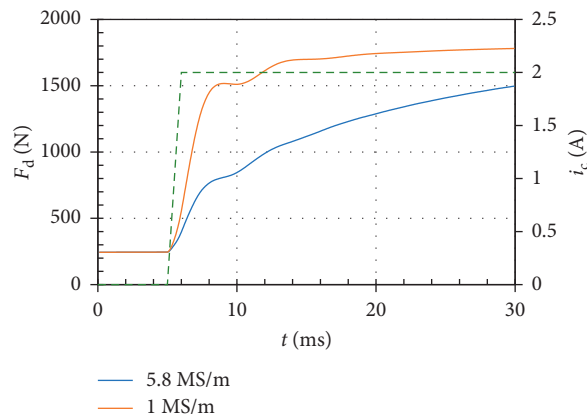


FIGURE 29: Core material’s electric conductivity: Full line: damping force time history; green dashed line: current step input. $H_c = 200$ A/m, $V_r = 0.3$ m/s.

- (vi) The electrical conductivity has a major influence on the dynamic behaviour of the actuator (Figure 29)
- (vii) The piston velocity influences the actuator’s response time. Low piston velocities degrade the response time in the current rise stage (Figures 30

and 32). It is likely due to the compressibility of the fluid (Figure 31).

The collected data enhance understanding the key mechanisms governing the flux/force output of MR

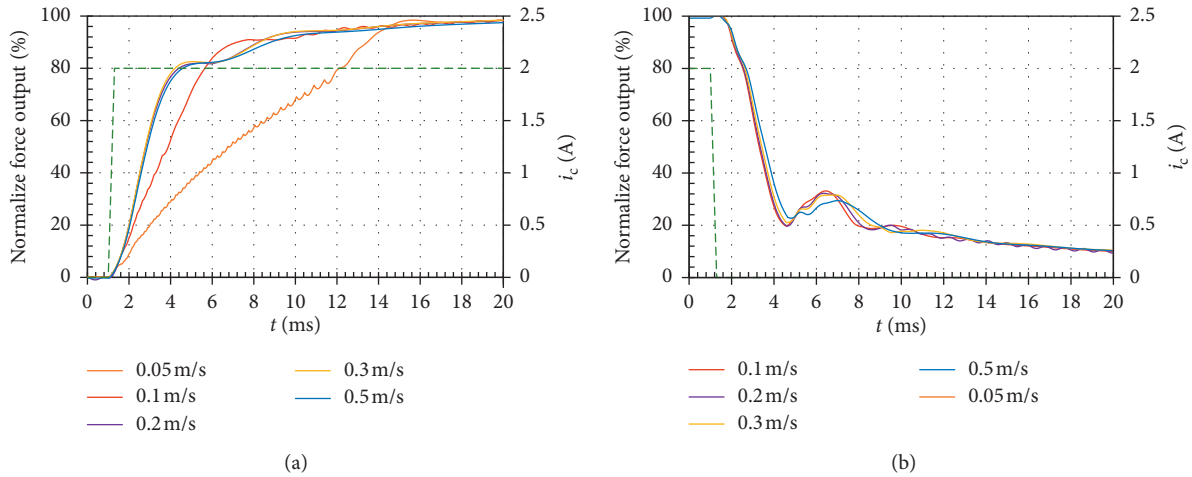


FIGURE 30: Influence of piston velocity for control current rise and drop (green dashed line) on the force output (full line). (a) Current rise. (b) Current drop.

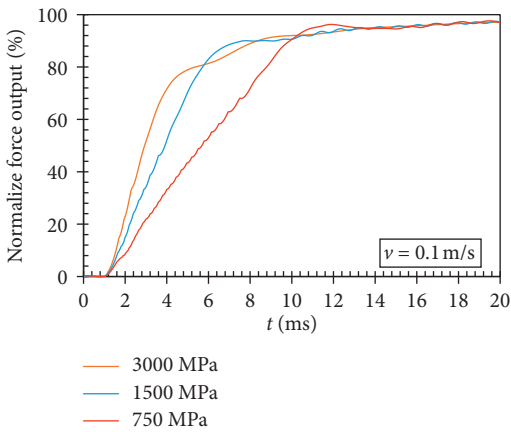


FIGURE 31: Influence of MR fluid bulk modulus on the force output at velocity 0.1 m/s.

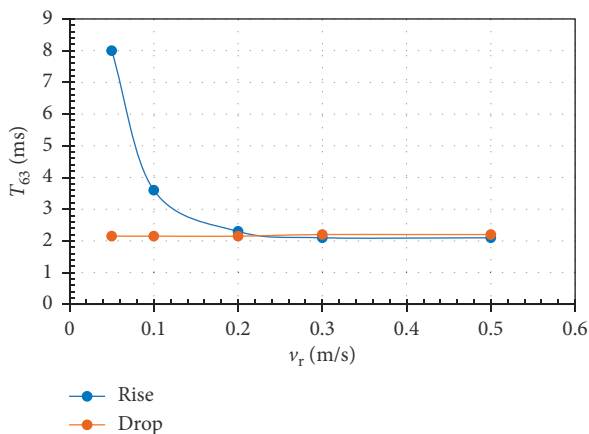


FIGURE 32: Influence of piston velocity on the primary response time for the rise and drop control current.

actuators. They allow for a clear separation of various contributors to the static and dynamic behaviour of such devices. In our opinion, the proposed model can be a useful

tool as it incorporates major key phenomena occurring in the actuator including magnetic hysteresis and remanence/coercivity, eddy currents, compressibility, and fluid inertia (hydraulic hysteresis), the MR effect. It allows separating the magnetic hysteresis from the hydromechanical one so that the two phenomena can be examined separately.

Data Availability

The data used to support the findings of this study are available from the corresponding author upon request.

Conflicts of Interest

The authors declare that they have no conflicts of interest.

Acknowledgments

The authors wish to acknowledge the support of the grant NAWA: E-Mobility and Sustainable Materials and Technologies (EMMAT) (number PPI/APM/2018/1/00027/U/001) sponsored by the Polish National Agency for Academic Exchange (NAWA).

References

- [1] J. Rabinow, "The magnetic fluid clutch," *Electrical Engineering*, vol. 67, no. 12, p. 1167, 1948.
- [2] J. Goldasz and B. Sapinski, *Insight into Magnetorheological Shock Absorbers*, Springer, Cham, Switzerland, 2015.
- [3] W. Kordonski and A. Shorey, "Magnetorheological (MR) jet finishing technology," *Journal of Intelligent Material Systems and Structures*, vol. 18, no. 12, pp. 1127–1130, 2007.
- [4] M. R. Jolly, J. W. Bender, J. D. Carlson, and L. Drive, "Properties and applications of commercial magnetorheological fluids," *Journal of Intelligent Material Systems and Structures*, vol. 10, no. 1, pp. 5–13, 1999.
- [5] A. Farjoud and E. A. Bagherpour, "Electromagnet design for magneto-rheological devices," *Journal of Intelligent Material Systems and Structures*, vol. 27, no. 1, pp. 51–70, 2016.

- [6] Z. Strecker, J. Roupec, I. Mazurek, O. Machacek, M. Kubik, and M. Klapka, "Design of magnetorheological damper with short time response," *Journal of Intelligent Material Systems and Structures*, vol. 26, no. 14, pp. 1951–1958, 2015.
- [7] Y.-M. Han, S.-B. Choi, and N. M. Wereley, "Hysteretic behavior of magnetorheological fluid and identification using Preisach model," *Journal of Intelligent Material Systems and Structures*, vol. 18, no. 9, pp. 973–981, 2007.
- [8] A. Sternberg, R. Zemp, and J. C. de la Llera, "Multiphysics behavior of a magneto-rheological damper and experimental validation," *Engineering Structures*, vol. 69, pp. 194–205, 2014.
- [9] C. P. Riley, "Effect of magnetic hysteresis in solenoid valve operation," *Sensor Letters*, vol. 11, no. 1, pp. 9–12, 2013.
- [10] Y. Chuang, S. Niu, S. L. Ho, W. Fu, and L. Li, "Hysteresis modeling in transient analysis of electric motors with AlNiCo magnets," *IEEE Transactions on Magnetics*, vol. 51, no. 3, pp. 1–4, 2015.
- [11] J. Goldasz, B. Sapinski, and Ł. Jastrzębski, "Assessment of the magnetic hysteretic behaviour of MR dampers through sensorless measurements," *Shock and Vibration*, vol. 2018, Article ID 3740208, 21 pages, 2018.
- [12] J. de Vicente, G. Bossis, S. Lacić, and M. Guyot, "Permeability measurements in cobalt ferrite and carbonyl iron powders and suspensions," *Journal of Magnetism and Magnetic Materials*, vol. 251, no. 1, pp. 100–108, 2002.
- [13] K. C. Pitman, "The influence of stress on ferromagnetic hysteresis," *IEEE Transactions on Magnetics*, vol. 26, no. 5, pp. 1978–1980, 1990.
- [14] J. Zheng, Y. Li, Z. Li, and J. Wang, "Transient multi-physics analysis of a magnetorheological shock absorber with the inverse Jiles–Atherton hysteresis model," *Smart Materials and Structures*, vol. 24, no. 10, pp. 1–16, 2015.
- [15] B. F. Spencer Jr., S. J. Dyke, M. K. Sain, and J. D. Carlson, "Phenomenological model for magnetorheological dampers," *Journal of Engineering Mechanics*, vol. 123, no. 3, pp. 230–238, 1997.
- [16] I. D. Mayergoyz, "Dynamic Preisach models of hysteresis," *IEEE Transactions on Magnetics*, vol. 24, no. 6, pp. 2925–2927, 1988.
- [17] B. D. Coleman and M. L. Hodgdon, "A constitutive relation for rate-independent hysteresis in ferromagnetically soft materials," *International Journal of Engineering Science*, vol. 24, no. 6, pp. 897–919, 1986.
- [18] D. C. Jiles and D. L. Atherton, "Theory of ferromagnetic hysteresis," *Journal of Magnetism and Magnetic Materials*, vol. 61, no. 1–2, pp. 48–60, 1986.
- [19] D. C. Jiles, J. B. Thoelke, and M. K. Devine, "Numerical determination of hysteresis parameters for the modeling of magnetic properties using the theory of ferromagnetic hysteresis," *IEEE Transactions on Magnetics*, vol. 28, no. 1, pp. 27–35, 1992.
- [20] A. Raghunathan, Y. Melikhov, J. E. Snyder, and D. C. Jiles, "Modeling the temperature dependence of hysteresis based on Jiles–Atherton theory," *IEEE Transactions on Magnetics*, vol. 45, no. 10, pp. 3954–3957, 2009.
- [21] K. Chwastek, "Frequency behaviour of the modified Jiles–Atherton model," *Physica B: Condensed Matter*, vol. 403, no. 13–16, pp. 2484–2487, 2008.
- [22] J. Tellinen, "A simple scalar model for magnetic hysteresis," *IEEE Transactions on Magnetics*, vol. 34, no. 4, pp. 2200–2206, 1998.
- [23] Y. M. Han, S. C. Lim, H. G. Lee, S. B. Choi, and H. J. Choi, "Hysteresis identification of polymethylaniline-based ER fluid using Preisach model," *Materials & Design*, vol. 24, no. 1, pp. 53–61, 2003.
- [24] P. Yadmellat and M. R. Kermani, "Adaptive modeling of a magnetorheological clutch," *IEEE/ASME Transactions on Mechatronics*, vol. 19, no. 5, pp. 1716–1723, 2014.
- [25] J. An and D.-S. Kwon, "Modeling of a magnetorheological actuator including magnetic hysteresis," *Journal of Intelligent Material Systems and Structures*, vol. 14, no. 9, pp. 541–550, 2003.
- [26] C. Jędrzycka, P. Sujka, and W. Szeląg, "The influence of magnetic hysteresis on magnetorheological fluid clutch operation," *COMPEL—International Journal for Computation and Mathematics in Electrical and Electronic Engineering*, vol. 28, no. 3, pp. 711–721, 2009.
- [27] P. Guo, J. Xie, and X. Guan, "Dynamic model of MR dampers based on a hysteretic magnetic circuit," *Shock and Vibration*, vol. 2018, Article ID 2784950, 13 pages, 2018.
- [28] J. Goldasz, B. Sapinski, and L. Jastrzębski, "On the application of Bouc–Wen hysteresis approach for modeling of MR actuators," in *Proceedings of the Actuator 16th International Conference on New Actuators*, pp. 1–5, Breme, Germany, June 2018.
- [29] S. M. Chen, W. A. Bullough, and J. Hart, "CFD study of the flow in a radial electrorheological fluid clutch," *Journal of Physics: Conference Series*, vol. 21, no. 15, pp. 1569–1574, 2010.
- [30] D. Lin, P. Zhou, and A. Bergqvist, "Improved vector play model and parameter identification for magnetic hysteresis materials," *IEEE Transactions on Magnetics*, vol. 50, no. 2, pp. 18–21, 2014.
- [31] J. Goldasz and B. Sapinski, "Nondimensional characterization of flow-mode magnetorheological/electrorheological fluid dampers," *Journal of Intelligent Material Systems and Structures*, vol. 23, no. 14, pp. 1545–1562, 2012.
- [32] Lord Company, <http://www.lordmrstore.com/lord-mr-products/mrf-132dg-magneto-rheological-fluid>.
- [33] M. Rosu, P. Zhou, D. Lin et al., *Multiphysics Simulation by Design for Electrical Machines, Power Electronics, and Drives*, John Wiley & Sons, Hoboken, NJ, USA, 2018.
- [34] D. Lin, P. Zhou, C. Lu, N. Chen, and M. Rosu, "Construction of magnetic hysteresis loops and its applications in parameter identification for hysteresis models," in *Proceedings of the 2014 International Conference on Electrical Machines (ICEM)*, pp. 1050–1055, Berlin, Germany, September 2014.
- [35] M. Rosu, *Advanced Hysteresis Modeling*, Ansys, Canonsburg, PA, USA, 2017.
- [36] N. M. Wereley and L. Pang, "Nondimensional analysis of semi-active electrorheological and magnetorheological dampers using approximate parallel plate models," *Smart Materials and Structures*, vol. 7, no. 5, pp. 732–743, 1998.
- [37] W. Hu and N. M. Wereley, "Nondimensional damping analysis of flow-mode magnetorheological and electro-rheological dampers," in *Proceedings of the ASME 2003 International Mechanical Engineering Congress and Exposition*, pp. 265–272, American Society of Mechanical Engineers, Washington, DC, USA, November 2003.
- [38] R. W. Phillips, *Engineering Applications of Fluids with a Variable Yield Stress*, University of California, Berkeley, CA, USA, 1969.
- [39] J. Goldasz and B. Sapinski, "Verification of magneto-rheological shock absorber models with various piston configurations," *Journal of Intelligent Material Systems and Structures*, vol. 24, no. 15, pp. 1846–1864, 2013.
- [40] Mathworks Matlab, <https://www.mathworks.com>.

- [41] M. Kubík, O. Machacek, Z. Strecker, J. Roupec, P. Novak, and I. Mazurek, "Transient magnetic model of magnetorheological damper and its experimental verification," *MATEC Web of Conferences*, vol. 153, article 06002, 2018.
- [42] Z. Strecker, M. Kubík, P. Vitek, J. Roupec, D. Paloušek, and V. Šreibr, "Structured magnetic circuit for magnetorheological damper made by selective laser melting technology," *Smart Materials and Structures*, vol. 28, no. 5, article 055016, 2019.
- [43] M. Kubík, O. Macháček, Z. Strecker, J. Roupec, and I. Mazurek, "Design and testing of magnetorheological valve with fast force response time and great dynamic force range," *Smart Materials and Structures*, vol. 26, no. 4, article 047002, 2017.

